Additive Manufacturing 37 (2021) 101608

Contents lists available at ScienceDirect

Additive Manufacturing

journal homepage: www.elsevier.com/locate/addma

Topology optimization of imperfect lattice materials built with process-induced defects via Powder Bed Fusion

Ahmed Moussa, David Melancon, Asma El Elmi, Damiano Pasini *

Mechanical Engineering Department, McGill University, Montreal, Quebec H3A0C3, Canada

ARTICLE INFO

Keywords:
Imperfect lattice materials
Topology optimization
Additive manufacturing
Powder bed fusion
Geometric defects

ABSTRACT

Lattice materials built via additive manufacturing feature process-induced defects that impact their mechanical properties and optimum design. This work presents a methodology to integrate geometric defects in a density-based formulation for topology optimization of additively built lattice materials. The method combines imperfect unit cell models capturing their geometric defects with a homogenization scheme upscaling their effective properties, into a topology optimization formulation. The method is of general application, and it is here demonstrated through the application to two cell topologies, the Tetrahedron-based and the Octet-truss unit cells, called to satisfy specific geometric constraints. Verification is performed through the solution of two well-known benchmark problems in 3D: the fixed-beam and the L-shaped beam, assumed to consist of either defect-free or imperfect lattice materials. The impact of process-induced defects, and cell orientation is demonstrated on the elastic anisotropy of the unit cell, the optimized gradients of relative density and the global compliance of the beams. The results highlight the significance of accounting for geometric defects in topology optimization of additively built lattice materials.

1. Introduction

Lattice materials can be designed to feature a range of optimally tuned physical properties, such as stiffness to mass ratio [1–3], thermal expansion control [4], heat transfer [5], band gaps [6], fluidic permeability [3,7,8], and mechanical biocompatibility [9–11], often superior to those of monolithic solids. Additive manufacturing (AM) technology provides ample freedom to generate complex architectures with controlled pore morphology and graded pore distribution [12,13]. Once manufactured, however, their geometries can deviate from their nominal counterpart due to process-induced defects appearing in both the base material and geometry. The outcome is an undesired shift in mechanical and functional performance [14]. In fluid transport applications, for example, pore occlusion and other defects caused by flawed material deposition can strongly penalize fluid permeability, flow profiles, and pressure drops [15–18]. In structural applications, process-induced defects can generate sizeable knock-down factors on the elastic properties and changes in their failure modes [19–21]. In bone replacement applications, overmelted struts can obstruct voids and lead to reduced porosity to an extent that negatively affects bone ingrowth and osteoconductive properties [10,11,22–27].

The defect sensitivity of lattice architectures depends on several factors, such as base material, geometric characteristics, manufacturing technology, and type of defect. Investigations on defect sensitivity have considered either predefined defects introduced by design, i.e. as-designed defects, or manufacturing-induced defects. In cellular materials, as-designed imperfections can be randomly dispersed, such as missing elements (struts, joints, or unit cells) and geometric irregularities (displaced nodes, and variable cross-section shape) [28,29], while other imperfections might also be periodically distributed. Examples of periodically-distributed defects include cell wall waviness, displaced nodes, plateau borders, and surface roughness [14]. Early works on cellular materials have focused on as-designed defects with the goal of studying their impact on their structural properties. For example, misplaced nodes and cell wall waviness are defects that reduce the elastic moduli of planar lattices [29]. Other works have studied their influence on yield [30], ductility [31], fracture toughness [32–34] and other properties.

For process-induced imperfections, material defects typically include inclusions, precipitates, or debris of a foreign matter, or material discontinuity such as voids, cavities, and cracks [14,35]. Sizeable deviations in the form of uneven material deposition have been observed

* Corresponding author.
E-mail address: damiano.pasini@mcgill.ca (D. Pasini).

https://doi.org/10.1016/j.addma.2020.101608
Received 25 February 2020; Received in revised form 3 August 2020; Accepted 10 September 2020
Available online 24 September 2020
2214-8604/© 2020 Elsevier B.V. All rights reserved.

for elements inclined differently with the building direction, a characteristic factor of lattice materials [36–39]. The consequence is typically a discrepancy in the expected mechanical and functional response at levels that depend on the relationship between the base material and length scale of the constituent elements. Even at small ranges, perturbations can generate unusual responses or deteriorate material functionality. For example, with elastoplastic architectures, geometric defects have imparted changes in the damage initiation and failure mechanisms that are not observed in their defect-free counterparts [19]. They can also lead to partial (or complete) pore closure with resulting changes in elastic moduli and strength [23]. Other works have also investigated the impact not only on the failure response [13,20,21,28,40–43], but also on the fatigue properties [44–46] of additively manufactured lattice materials. For instance, a reduction has been observed in fatigue resistance of manufactured lattice structures, due to the non-uniform material distribution built up at sharp-notched junctions which generate significant stress peaks [38].

Several works have used topology optimization to design structures with functionally-graded lattice materials with enhanced mechanical and functional performance [47–51]. Others have focused on imposing constraints, such as buckling [52,53] and stress constraints [54,55], to prevent the failure of lattice materials. These works typically model nominal architectures that are free of manufacturing defects. Their tailored design may function well in ideal settings, but they might fail unexpectedly when micro imperfections and small load perturbations are present. Their use in practical applications, therefore, might become limited [56]. To address this issue, recent efforts have been made to incorporate uncertainties in load, geometry and material properties (resulting from manufacturing), into the design of architected materials. An example is the development of robust design strategies for cellular materials that account for imperfections at the connection between cells, as well as for wall thickness variations [57]. Robust topology optimization [58,59] is also another effective tool that has been used to design auxetic materials featuring small size hinges that facilitate rotation to maximize auxetic effects [60]. In such materials, small variation in thickness may result in disconnected features that can significantly decrease the elastic stiffness [60,61]. Statistical modelling for uncertainty quantification has also been introduced to design additively manufactured single-material lattices [62]. Recently, a robust approach has been used to design multi-material lattice structures under given combinations of material and load uncertainties [63]. To date, however, the impact of AM induced geometric defects on the mechanics and optimized porosity gradient of porous materials has not been so far studied.

This work addresses the role of a set of manufacturing defects on the mechanics and density distribution of optimally graded 3D lattices. We combine a density-based formulation for topology optimization with imperfect cellular models that are statistically equivalent in defect distribution to their as-built counterparts (see Section 2). The presented methodology is general, and here exemplified through the use of two high-strength unit cells (the Tetrahedron-based and the Octet-truss) previously investigated for load-bearing bone replacement applications [64]. We use asymptotic homogenization to upscale their effective elastic properties at given cell orientations as a function of relative density. In Section 3, the final compliance and optimized relative density distribution are compared for imperfect and defect-free models, to assess the effect of AM defects, unit cell orientation, and cell topology, followed by a discussion of the findings and limitations of this work.

2. Methodology

One path to optimize the porosity gradients of a cellular material with defects is to use a robust approach that searches for defect-insensitive architectures. In this paper, we adopt an alternative deterministic strategy that accounts for defects and integrate their impact on the elastic properties. We first develop homogenized models for additively built lattices featuring a statistical dispersion of process-induced defects, and then we formulate a gradient-based topology optimization problem for imperfect architectures. The proposed methodology is of general application, and here applied for demonstrative purposes to a cellular material subject to geometric constraints imposed by a bone replacement application. Fig. 1 summarizes the key steps underpinned by notions of multiscale mechanics of imperfect lattices and topology optimization.

- *Initialization of the design space.* The design domain Ω is constructed and discretized into solid elements, each representing a unit cell making up the lattice domain (Fig. 1).
- *Unit cell selection, manufacturing, and characterization.* A unit cell is selected a priori from an available pool of cell topologies and used to generate lattice material samples for additive manufacturing. Here, two representative cells, the Tetrahedron-based and Octet-truss topologies, are chosen for demonstrative purposes. Their geometric features are restricted within the allowable design space of bone replacement implants, which satisfy both additive manufacturing and pore size requirements for bone ingrowth. This translates into inequality geometric constraints on porosity, pore size, and strut thickness [23,64].
- *Generation of imperfect-geometry representative models.* The additively manufactured lattice samples are μCT-reconstructed and morphologically characterized to attain the dispersion of a set of SLM-induced geometric defects. These include: (1) the change in strut thickness t, and (2) the deviation of the center axis, c_d, from the principal axis of an ideal strut. Their probabilistic distribution is integrated into imperfect-architecture models that can represent behavior of as-built porous biomaterials. The method of Asymptotic Homogenization (AH) [65] is employed to calculate their homogenized elastic properties, as a function of relative density ρ, along given orientations of the unit cells relative to the building direction. The design variable ρ is initially assumed to be uniform within the design domain.
- *Finite element solver.* Finite element analysis (FEA) is used to solve the boundary value problem of a deformable body subjected to a traction τ at the traction boundary Γ_τ, a displacement d at the displacement boundary Γ_d, and a body force f.
- *Topology optimization.* A gradient-based formulation is used to find the optimized distribution of relative density that minimizes the objective function, in this representative compliance case, for a prescribed total amount of material [66]. Both as-designed, used as baseline, and imperfect models are examined for comparative purposes. The Method of Moving Asymptotes (MMA) is used to update the design variables ρ [67], which are then filtered using a density filter [68]. The nodal displacements and the unit cell's effective properties are first obtained to create the global stiffness tensor. Then, the gradients of the objective function and constraints are calculated. The process of optimization continues until the achievement of the optimized relative density distribution that fulfils both the objective and the constraints.

2.1. Unit cell selection, additive manufacturing, and μCT-reconstruction

We exemplify the general methodology here presented by applying it to a class of lattice materials whose geometric parameters satisfy a set of constraints, typically used for the design of porous bone replacement implants. Recent works on AM of porous biomaterials have studied the interaction between manufacturability and bone ingrowth, a relation that can be expressed by placing specified constraints on the geometry of the unit cell [10,64]. Fig. 2 illustrates the allowable design space for the defect-free Tetrahedron-based (a) and Octet-truss (b) cells. Such cell topologies are chosen due to their stretch-dominated deformation mode. This endows the necessary structural capacity (stiffness) for using them

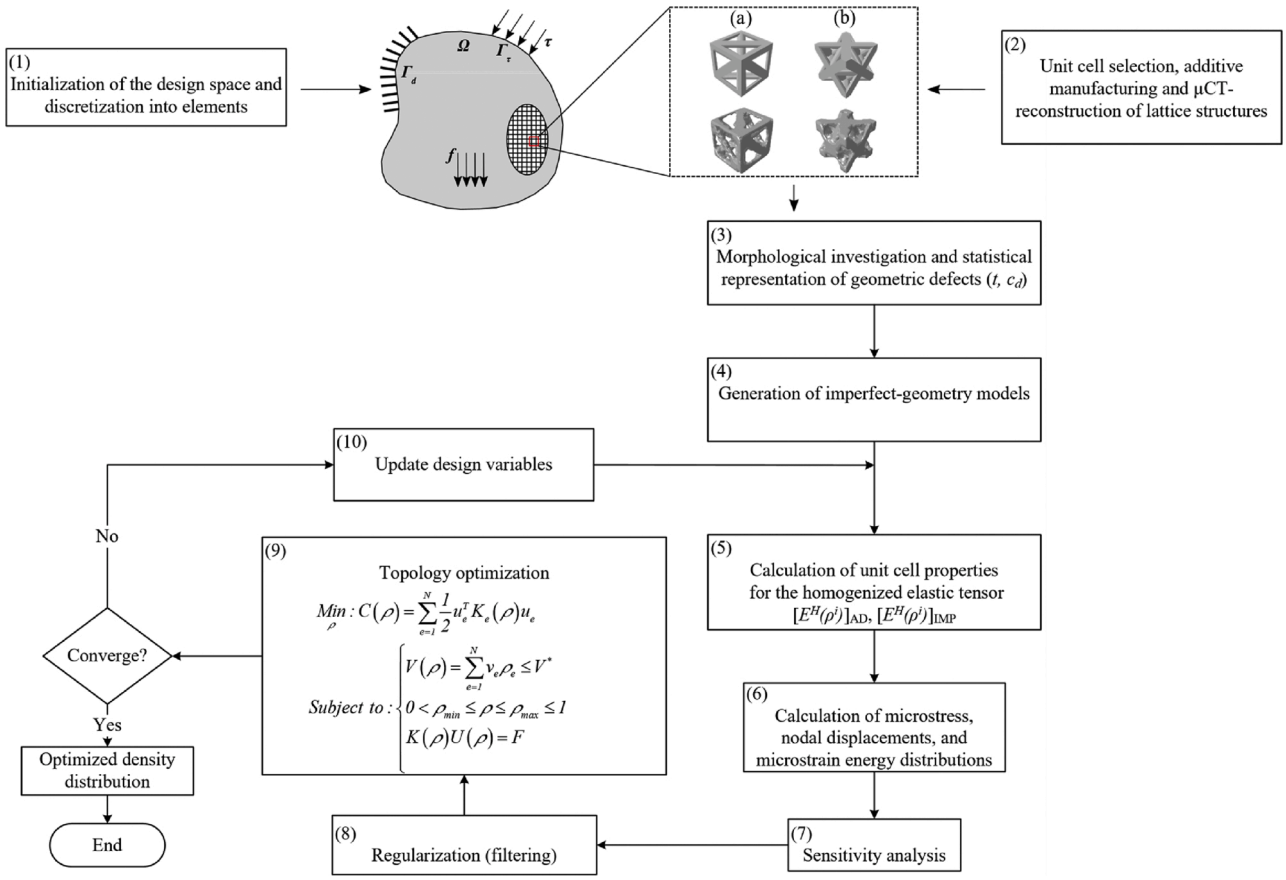

Fig. 1. Flow chart illustrating the design scheme here presented to optimally grade a cellular domain with predefined unit cells additively built with imperfect-geometry. $[E^H(\rho^i)]_{AD}$ and $[E^H(\rho^i)]_{IMP}$ are the as-designed and imperfect homogenized elasticity tensors.

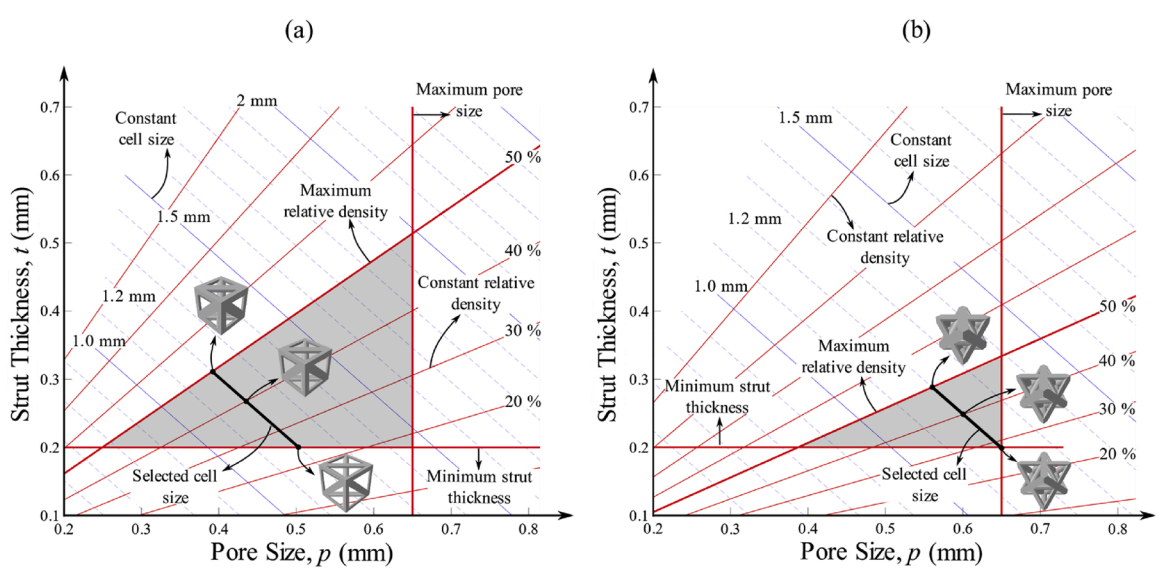

Fig. 2. Visualization of bone ingrowth and additive manufacturing constraints of the as-designed Tetrahedron-based (a), and Octet-truss (b) unit cells. Thick black lines represent unit cells of l =1.2 mm selected for this study.

in load-bearing orthopaedic applications [64,69]. Further, these unit cells have been used to design biomaterials with improved bone ingrowth [64], as well as to develop architected implants with optimized porosity gradients [10,11,26]. The design space of each unit cell (Fig. 2), is constructed by lines of constant relative density, ρ, and cell size, l, defined with respect to pore size, p, and the thickness of strut, t, with circular cross-section. The pore size is here defined as the largest sphere that can pass within two adjacent cells in a periodic lattice [64]. By imposing bone ingrowth requirements ($50 \leq p \leq 650$ µm and $\rho \leq 0.5$ [23,70,71]) along with manufacturing constraints ($t \geq 200$ µm), a triangular domain arises with boundaries and area that depend on cell topology. This represents the allowable design space of a unit cell (grey

area) and includes all the geometric parameters that are both manufacturable with the current AM technology capabilities and conducive to osseointegration [64]. Here, we prescribe a cell size of $l = 1.2$ mm (black line), a choice that translates in relative density ranges for the Tetrahedron-based and Octet-truss cells between respectively $0.25 \leq \rho \leq 0.5$ and $0.28 \leq \rho \leq 0.5$, pore size between $390 \leq p \leq 510$ and $560 \leq p \leq 650$ μm, and strut thickness between $0.2 \leq t \leq 0.3$ and $0.2 \leq t \leq 0.28$ mm.

To explore the design space of the selected cell topologies, we consider a set of experimental data used in a previous study [23] where 160 titanium alloy (Ti-6Al-4 V) porous samples are additively built with Selective laser melting (SLM). From the sample set, 16 points tracing the boundaries and covering the area of the admissible design spaces are selected and built (nine Tetrahedron-based and seven Octet-truss lattices) [23]. A typical sample of each design geometry is then scanned using a SkyScan 1172 high-resolution μCT to produce the CT-scan data required to reconstruct the lattices. Fig. 3 shows an example of as-designed, as-manufactured, and full μCT-reconstructed lattice samples, with a zoom on a μCT-reconstructed unit cell. Geometry reconstruction is performed via a semi-automated segmentation process using ITK-SNAP [72].

2.2. Generation of imperfect-geometry models using statistical representation of geometric defects

To generate numerical models that can predict the mechanical properties of as-built microarchitectures, we investigate a set of SLM-induced geometric defects. In Fig. 3 (d), the dashed lines show a clear disparity between as-designed and as-manufactured cells with mismatches that are strongly dependent on the strut angle [36,38]. Further evidence is given in Fig. 4, showing scanning electron microscopy (SEM) images of an Octet-truss representative sample. In this work, two AM defects are considered: (1) non-uniform strut thickness t (Fig. 4 (a)), and (2) center deviation of the ideal strut axis c_d (Fig. 4 (b)). To consider them in our numerical models, the reconstructed struts are grouped into sets with respect to their orientation over to the build plane. The Tetrahedron-based cell has three different strut orientations (horizontal, vertical, and diagonal), while the Octet-truss cell has two (horizontal and diagonal). The geometry of each strut is sliced with a sequence of parallel planes normal to the as-designed strut axis. We account for the first geometric imperfection by fitting a circle through the points on each plane and calculating its mean radius. Then for the center deviation, the offset of the center of each fitted circle is calculated about the axis of the ideal strut. Finally, a probability distribution of each geometric imperfection is constructed using the data obtained from the statistical analysis of the defects.

First, a convergence analysis is performed to verify that the sample size of struts selected at different orientations is sufficient and descriptive in capturing the distribution of the defects [19]. For example a representative octet sample is reconstructed by randomly selecting at least 5% of the horizontal struts and 3% of the diagonal struts to generate probability density distributions of geometric defects. Using a Kernel density estimate [73], each probability distribution is fitted to a probability density function. Then, we calculate the mean value and standard deviation of geometric defects, to statistically quantify the probability distributions. This process enables the generation of a pool of numerical data, i.e. a library of strut thicknesses and center deviations, that parallel the imperfection distributions. Using the probability density distributions, an in-house code is built to generate numerical models with imperfect porous architecture that is statistically equivalent to that of the as-manufactured counterpart (see Fig. 5). The method of integrating manufacturing defects into numerical models is computationally effective and recent research works have demonstrated its ability to accurately capture the mechanical behavior of lattices manufactured with SLM [19,23].

2.3. Mechanical properties of lattice materials

The calculation of the effective properties of lattice materials through homogenization is well established in the literature. Here we resort to Asymptotic Homogenization (AH), one among other methods [74,75], widely used in the field of lattice materials [11,26,65,76–79].

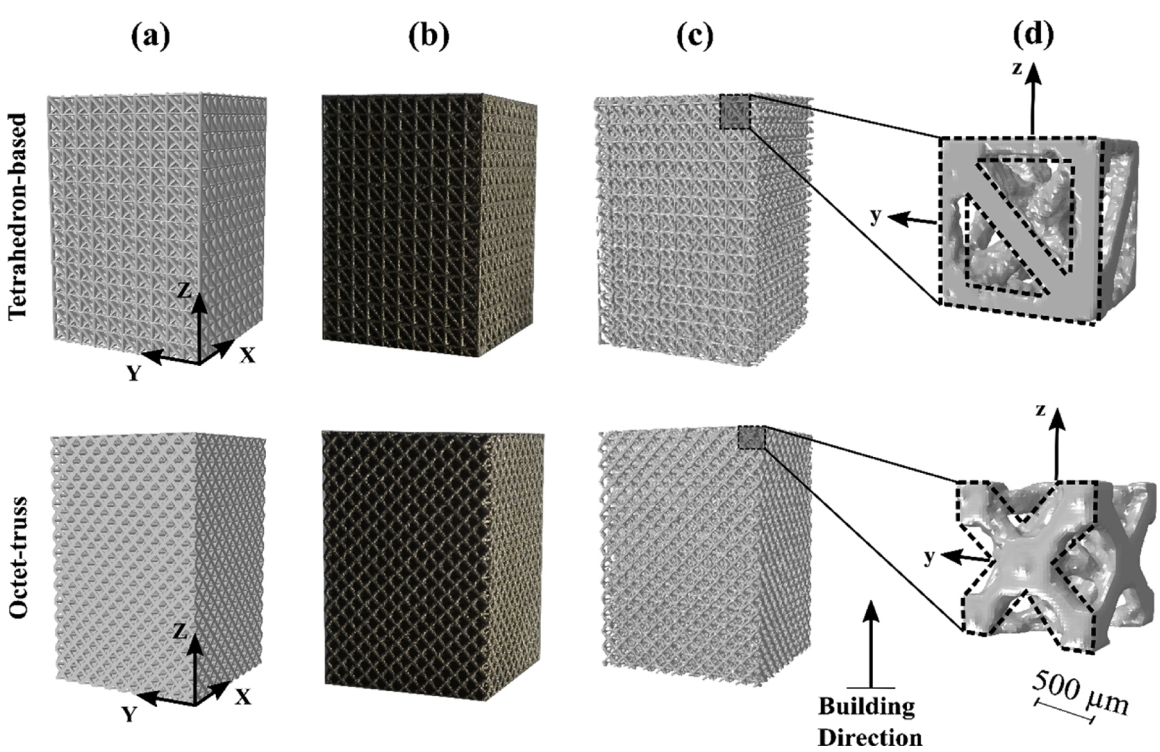

Fig. 3. (a) as-designed, (b) as-manufactured, and (c) μCT-reconstructed lattice samples; (d) μCT-reconstructed Tetrahedron-based and Octet-truss unit cells showing geometric mismatches with their as-designed counterpart (dashed lines).

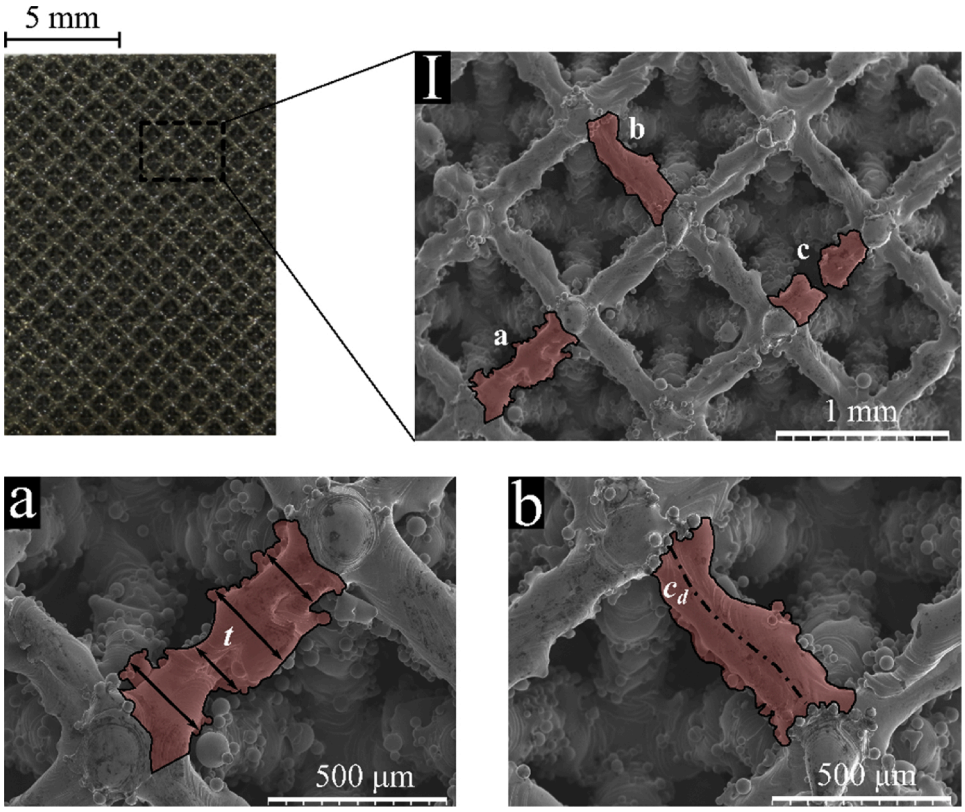

Fig. 4. Top-left: as-manufactured Octet-truss sample. (I) SEM images with SLM manufacturing defects highlighted: non-uniform cross-sectional shape and thickness t (a), center deviation of the strut axis c_d (b), and broken strut (c), a defect type not considered in this work.

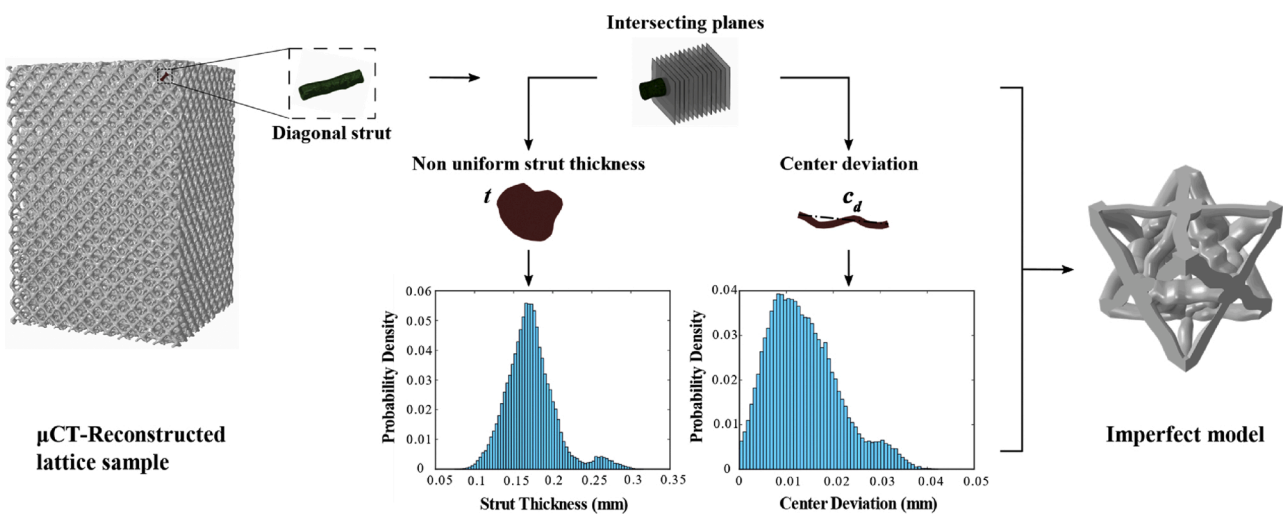

Fig. 5. Scheme used to quantify the dispersions of strut thickness and center deviation and their integration into imperfect models. The Octet-truss sample with 40 % relative density is shown as an example.

We apply AH to calculate the effective properties (i.e. the homogenized elasticity tensor) of the Tetrahedron-based and Octet-truss cells, using the as-designed (nominal) and imperfect models under their prescribed range of relative density (Fig. 2). For the Tetrahedron-based topology, six elastic constants are required to define the stiffness tensor (see Appendix A). The cubic symmetry of the Octet-truss yields a stiffness tensor dependent on three elastic constants only: Young's modulus, E_{ii}, shear modulus, G_{ij}, and Poisson's ratio, υ_{ij}. Fig. 6 shows the effective Young's and shear moduli of as-designed ($[E_{ii}]_{AD}$, $[G_{ij}]_{AD}$) versus imperfect ($[E_{ii}]_{IMP}$, $[G_{ij}]_{IMP}$) models for Tetrahedron-based (top) and Octet-truss (bottom) unit cells. The elastic properties are normalized with the bulk properties of the isotropic (heat-treated) titanium alloy (Ti6Al4V) previously tested ($E_s = 114$ GPa and $\upsilon_s = 0.342$) [80], and expressed as a function of relative density ρ. A clear discrepancy of elastic properties appears in Fig. 6 between as-designed and imperfect models. The maximum differences in Young's and shear moduli are 23 % and 18 % for the Tetrahedron-based unit cell, and 21 % and 39 % for the Octet-truss topology.

The geometric discrepancy as well as specific symmetry in elastic properties of each unit cell have a directional impact on the unit cell

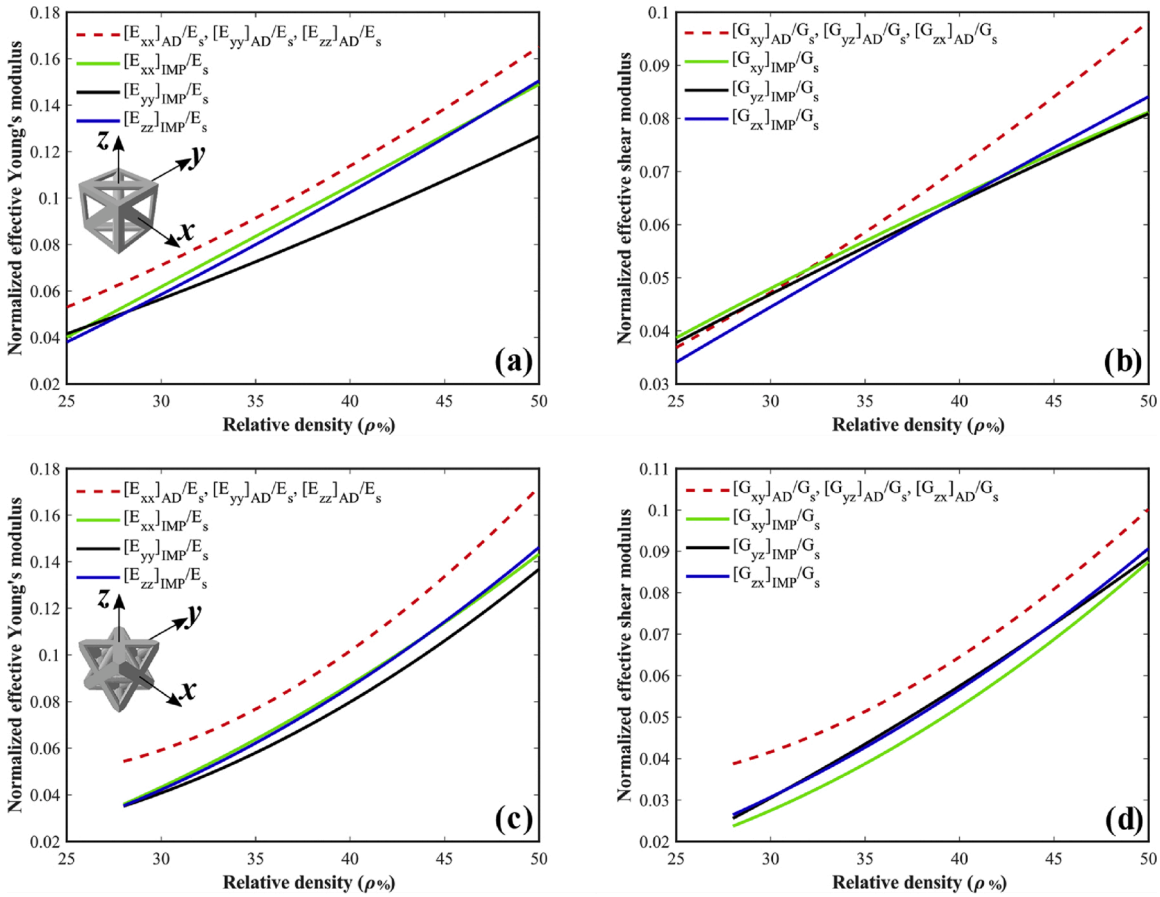

Fig. 6. Normalized effective properties as a function of relative density of as-designed versus imperfect models for Tetrahedron-based (a, b), and Octet-truss (c, d) unit cells at cell size=1.2 mm.

response, which also influences the optimized distribution of relative density throughout the entire cellular domain. To capture the moduli dependency on cell orientation with respect to the building direction, Figs. 7 and 8 illustrate three-dimensional and planar polar plots of the elastic moduli, while Figures D.1 and D.2 show those of the shear moduli. The responses are given for the Tetrahedron-based and Octet-truss unit cells at $\rho = 0.4$ (i.e. 60 % porosity), value here taken as representative of the admissible design space (Fig. 2). Manufacturing defects lead to a shift in symmetry and reduction in elastic moduli of as-built architectures, observations aligned with findings in the literature [20,38,43]. In the planar plots of the Young's modulus, the maximum discrepancy in the x direction, $\Delta(E_{xx}/E_s)_{\max}$ between as-designed and imperfect models is 23 % for the Tetrahedron-based at 60 degrees and 25 % for the Octet-truss cells at 45 degrees rotation angle around z-axis. More details about polar plots are given in Appendices C and D.

2.4. Topology optimization

Approaches for robust topology optimization exist in the literature to handle manufacturing imperfections and assess their role on the optimized design. One of them is the worst-case scenario, where manufacturing imperfections are typically allowed to vary in a specified interval, and the structure with the worst performance is considered in the optimization [59,61,81]. This strategy, however, is often over-conservative and does not use a realistic representation of the manufacturing defects that emerge during a specific manufacturing process [14,81]. Other methods use a robust formulation, where probabilistic measures are introduced to model non-uniform manufacturing defects, such as material and geometric uncertainties [82–85]; in these cases, a probability distribution is typically assigned to the uncertain parameters, and the objective function is defined as a weighted average of the mean value of a given structural metric, along with its standard deviation [82].

In this work, we adopt an alternative approach of topology optimization that is deterministic and account for a realistic representation of manufacturing defects along with their impact on the elastic properties of the lattice domain. The probability distribution of defects is obtained from CT-scan data of as-built lattice samples, and their statistical modelling is done only once to generate numerical models with imperfect porous architecture, prior to the start of the optimization process (see section 2.2. and the flow chart in Fig. 1). Then the homogenized elasticity tensor of a given imperfect unit cell is calculated for each relative density, and used as an input in the deterministic formulation of topology optimization (Fig. 1). The advantages of this strategy are the reduced computational cost and the treatment of actual defects without relying on any pre-defined distribution.

In Sections 2.4.1 and 2.4.2 the problem formulation and the filtering technique used are presented, while the sensitivity analysis is discussed in Section 2.4.3.

2.4.1. Problem formulation

In this work, we minimize the compliance for a prescribed total amount of material, under given conditions of support and loading to find the optimized density distribution through the design domain. The design domain is discretized into solid elements, where one design variable (i.e., relative density ρ) is allocated for each element. The design variables are used to construct the design vector. As discussed above in Section 2.2 and Fig. 2, for constant cell size, the relative density of a unit cell is controlled by the strut thickness t and pore size p. A final design is thus achieved with ranges of density distribution satisfying

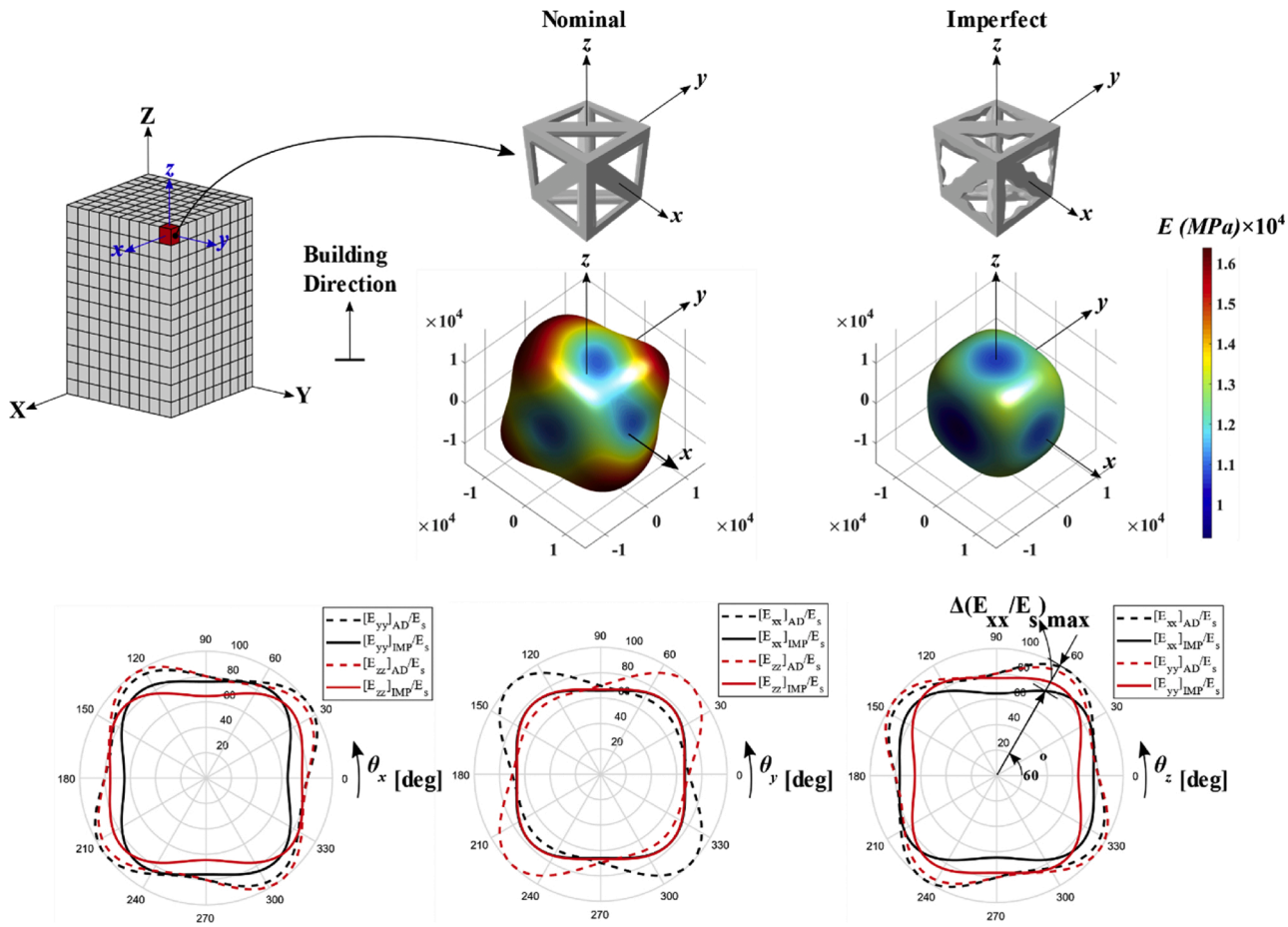

Fig. 7. 3D polar plots of Young's moduli (top), and 2D polar plots (bottom) of the normalized Young's moduli along x, y, and z axes at given unit cell orientations, of as-designed (nominal) and imperfect models for the Tetrahedron-based topology, at relative density $\rho = 0.4$.

manufacturing, and bone ingrowth constraints, as shown in Fig. 2 for the Tetrahedron-based and Octet-truss cells. The mathematical problem formulation is generally expressed as:

$$\underset{\rho}{\text{Min}} : C(\rho) = \sum_{e=1}^{N} \frac{1}{2} u_e^T K_e(\rho) u_e$$

$$Subjectto : \begin{cases} V(\rho) = \sum_{e=1}^{N} v_e \rho_e \leq V^* \\ 0 < \rho_{\min} \leq \rho \leq \rho_{\max} \leq 1 \\ K(\rho)U(\rho) = F \end{cases} \tag{1}$$

wherein, ρ_e is the relative density of each element e corresponding to given strut thickness t and pore size p (Fig. 2), $V^*$is the prescribed volume fraction constraint of the solid material, v_e is the element volume, and N is the total number of elements. K is the global stiffness matrix of the structure, F is the global force vector, and $U(\rho)$ is the global vector of nodal displacements, the state variables. The values of ρ_{min} and ρ_{max} depend on the selected cell topology (Section 2.2); for the Tetrahedron-based topology $0.25 \leq \rho \leq 0.5$, and for the Octet-truss cell $0.28 \leq \rho \leq 0.5$.

2.4.2. Filtering of design variables

Filtering techniques are among other methods used to eliminate numerical instabilities and to ensure manufacturability of the optimized structure [86,87]. In this work, the density filtering method is used [68], among several techniques [88]. Each element density is recalculated as a weighted average of the densities of the neighborhood elements within a specified filter radius R. The element density ρ_i is updated to the filtered density $\tilde{\rho}_e$ as follows:

$$\tilde{\rho}_e = \frac{\sum_{i \in N_e} w(x_i) v_i \rho_i}{\sum_{i \in N_e} w(x_i) v_i} \tag{2}$$

wherein N_e is the neighborhood of element e, v_i is the volume of element i, and $w(x_i)$ is a weighting function that is given as:

$$w(x_i) = R - \|x_i - x_e\| \tag{3}$$

where, $x_i$and x_e are the central coordinates of elements i and e respectively.

2.4.3. Sensitivity analysis

The first-order derivatives (sensitivity information) of both objective function and constraints are necessary for the optimizer, to solve the optimization problem. The compliance sensitivity, reported in the literature [66,89], with respect to the variation of element density ρ_e is calculated as:

$$\frac{\partial C(\tilde{\rho})}{\partial \rho_e} = \sum_{i=1}^{Ne} \frac{\partial C(\tilde{\rho})}{\partial \tilde{\rho}_i} \frac{\partial \tilde{\rho}_i}{\partial \rho_e} \tag{4}$$

The derivatives of the filtered density with respect to the design variable, $\partial \tilde{\rho}_i / \partial \rho_e$, are expressed as:

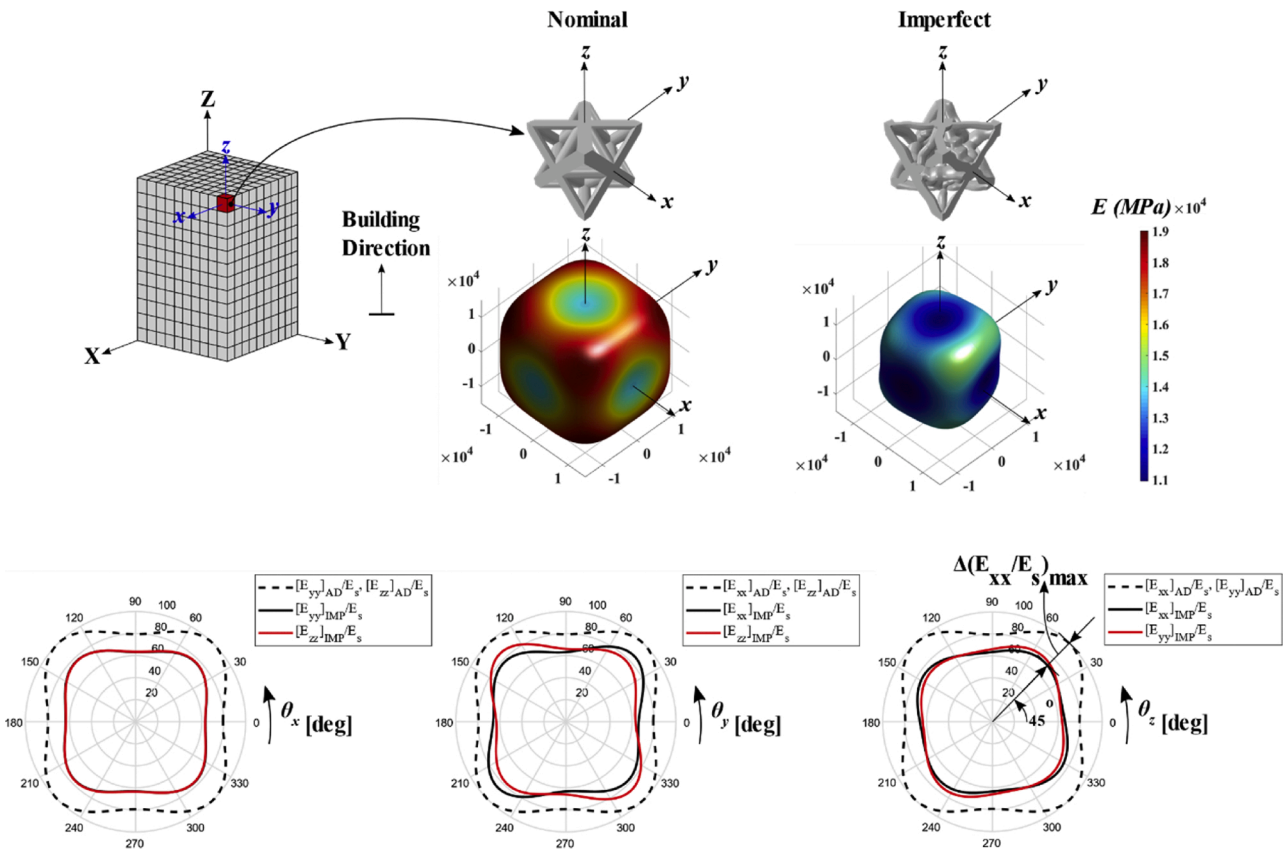

Fig. 8. 3D polar plots of Young's moduli (top), and 2D polar plots (bottom) of the normalized Young's moduli along x, y, and z axes at different unit cell orientations, of as-designed (nominal) and imperfect models for the Octet-truss topology, at relative density $\rho = 0.4$.

$$\frac{\partial \tilde{\rho}_i}{\partial \rho_e} = \frac{w(x_e)v_e}{\sum_{j \in N_i} w(x_j)v_j} \tag{5}$$

The compliance sensitivity with respect to the filtered density, $\partial C(\tilde{\rho})/\partial \tilde{\rho}_e$, is written in its final form as:

$$\frac{\partial C(\tilde{\rho})}{\partial \tilde{\rho}_e} = -\frac{1}{2} U^T(\tilde{\rho}) \frac{\partial K(\tilde{\rho})}{\partial \tilde{\rho}_e} U(\tilde{\rho}) \tag{6}$$

In the above expression, the derivatives of the global stiffness matrix with respect to the filtered density, $\partial K(\tilde{\rho})/\partial \tilde{\rho}_e$, are calculated through the assembly of the elemental stiffness matrix derivatives, $\partial K_e(\tilde{\rho})/\partial \tilde{\rho}_e$. Using the Gauss quadrature rule for volume integration, and for an eight-node brick solid element in the *rst* natural coordinate system with eight Gauss integration points, $\partial K_e(\tilde{\rho})/\partial \tilde{\rho}_e$ is written as:

$$\frac{\partial K_e(\tilde{\rho})}{\partial \tilde{\rho}_e} = \sum_{k=1}^{n_{gp}=8} w_k B_{rst}^T(r_k, s_k, t_k) \frac{\partial E^H(\tilde{\rho})}{\partial \tilde{\rho}_e} B_{rst}(r_k, s_k, t_k)|J| \tag{7}$$

where n_{gp} is the number of Gauss integration points in the parent element, w_k is the weight of the Gauss point k, B is the strain-displacement matrix, and J is the Jacobian matrix. $E^H(\tilde{\rho})$is either the as-designed or imperfect homogenized elastic tensor of each element e (Appendix A), which is calculated using AH at different unit cell orientations, as a function of relative density.

The derivatives of the material volume V with respect to the element density ρ_e are given as:

$$\frac{\partial V(\tilde{\rho})}{\partial \rho_e} = \sum_{i \in Ne} \frac{\partial V(\tilde{\rho})}{\partial \tilde{\rho}_i} \frac{\partial \tilde{\rho}_i}{\partial \rho_e} \tag{8}$$

Here, $\partial V(\tilde{\rho})/\partial \tilde{\rho}_i$ is found as:

$$\frac{\partial V(\tilde{\rho})}{\partial \tilde{\rho}_i} = v_s \tag{9}$$

where, $v_s$is the volume of the base solid element. The sensitivity analysis, which directs the search path to the optimized solution, is followed by solving the optimization problem using the MMA optimizer [67] until convergence is reached. Convergence plots are given in Appendix B.

3. Numerical examples and discussion

In this section, we examine the role of geometric defects, cell topology, and unit cell orientation on the compliance and optimized relative density distribution. We solve two benchmarks problems in 3D (fixed beam and L-shaped beam (Fig. 9)), and compare the solutions provided by the as-designed and imperfect unit cells. To study the impact of cell topology, we consider both the Tetrahedron-based and Octet-truss cell (effective properties in Figs. 6–8), each with its own specific number and orientation of struts. We also investigate the role of cell orientation on the final compliance and optimized density distribution.

Fig. 9 shows the two design domains (L=6 mm), boundary conditions, and external loads (vertical distributed load $F = 1500$ N). In both the problems, the design domain is discretized into elements with a size of 1.2 mm (Fig. 2), each representing a unit cell of the lattice. Eight-node brick elements are selected for the mesh, resulting in 48,000 elements and 54,571 nodes for the fixed-beam, and 165,375 elements and 176,256 nodes for the L-shaped beam. Heat-treated Ti6Al4V alloy (E_s = 114 GPa, Poisson's ratio $\upsilon_s = 0.342$ [80]) is used as base material. The structures are analyzed with the FEA software package ANSYS® (Canonsburg, Pennsylvania, U.S.A).

A design variable filter is applied with a filter radius of 1.5 times the

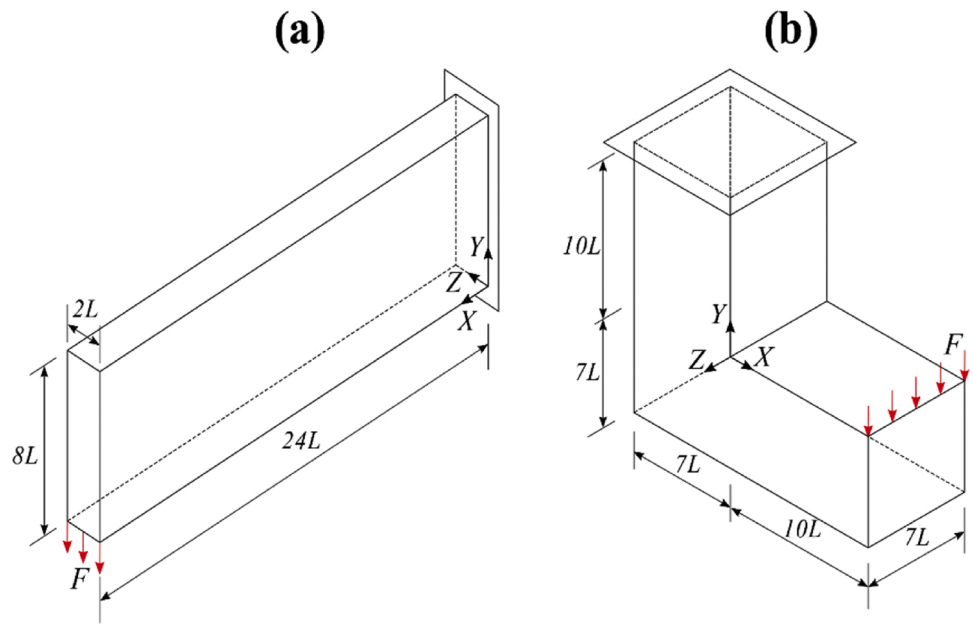

Fig. 9. Design domain, boundary conditions, and external loads for the optimization of (a) Fixed-beam, and (b) L-shape beam.

element size. The optimization problem is solved until convergence is reached for prescribed volume fractions V^* of the solid material, i.e. 37.5 % for the Tetrahedron-based cell and 39 % for the Octet-truss unit cell. To satisfy manufacturing and bone ingrowth constraints (Fig. 2) as well as to reduce the computational cost, the effective properties for both the defect-free and imperfect geometries are used during the optimization process.

3.1. Tetrahedron-based topology

Figs. 10 and 11 show the results of the two benchmark problems solved with the Tetrahedron-based topology. Two cell orientations are examined, at rotation angles 0 (top) along the build direction and 60 degrees (bottom) around the z-axis. The latter is chosen as a representative value to show the sensitivity to imperfections; in this case it represents the maximum discrepancy in Young's modulus (Fig. 7) along the x-direction, ($\Delta(E_{xx}/E_s)_{\max} = 23\%$).

Fig. 10 shows the compliance and optimized relative density distribution for the fixed beam problem. A range of insights on considering the process-induced defects (Fig. 4) can be gained by comparing the results of as-designed and imperfect models. Along the build direction (top), the compliance is 19 % higher for the imperfect model, but the difference in density distribution is mild. This difference can be attributed to the small discrepancies in Young's and shear moduli, E_{xx} and G_{xy}, the properties most relevant to this problem, where $\Delta(E_{xx}/E_s) = 4\%$ and $\Delta(G_{xy}/G_s) = 10\%$ (Fig. 7 and Figure D.1). At 60 degrees (bottom), the difference in density distribution is more pronounced, with less porosity in the middle region and 30 % higher compliance for the imperfect model.

For the as-designed models, although we observe a similar density

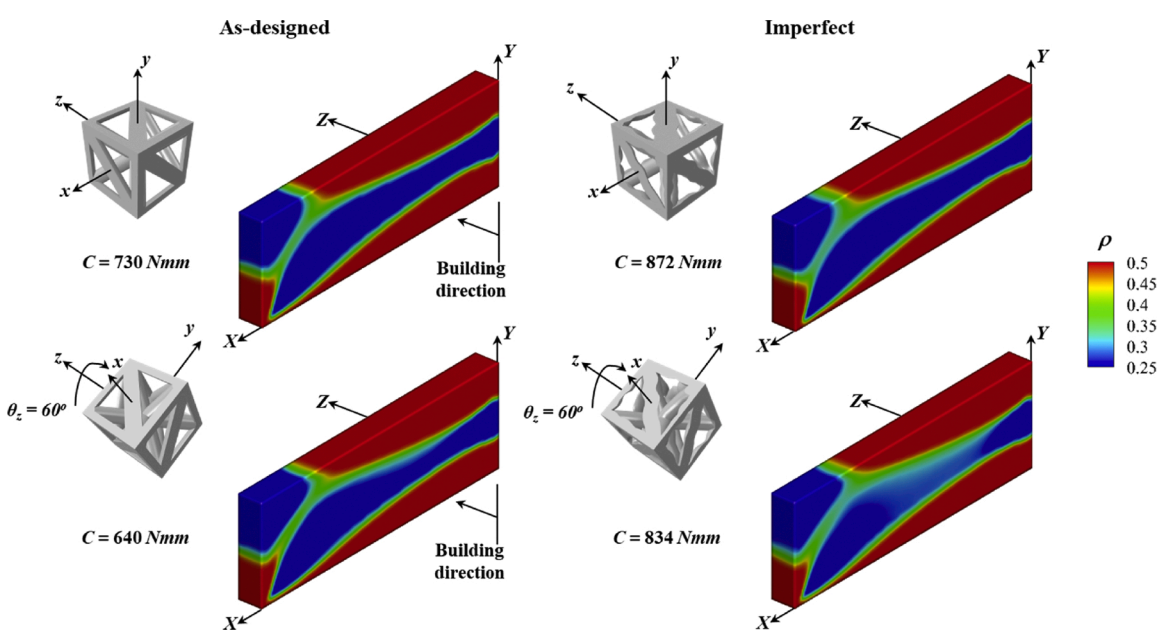

Fig. 10. Optimized relative density distribution for the fixed-beam benchmark problem, of as-designed versus imperfect models using the Tetrahedron-based topology. Top: unit cells rotated with an angle 0°, and bottom: unit cells rotated with an angle 60° around the z-axis.

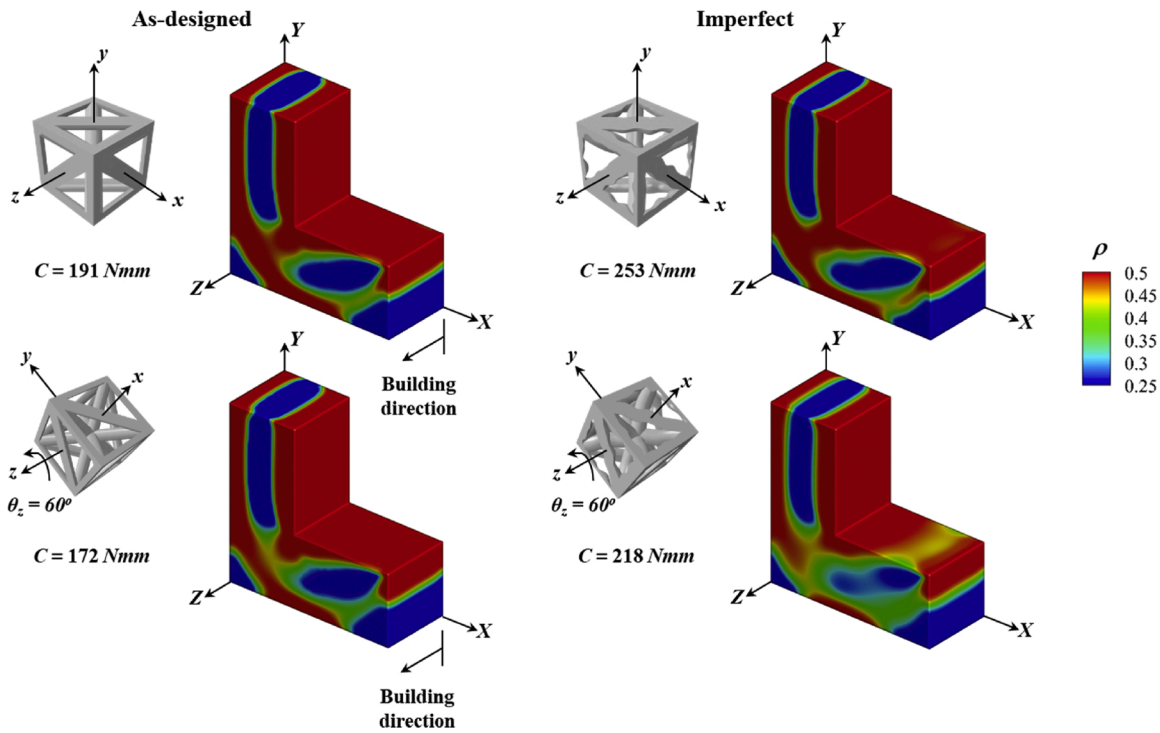

Fig. 11. Optimized relative density distribution for the L-shaped beam benchmark problem, of as-designed versus imperfect models using the Tetrahedron-based topology. Top: unit cells rotated with an angle 0°, and bottom: unit cells rotated with an angle 60° around the *z*-axis.

gradient for both cell orientations, there is a 12 % difference in compliance. This can be attributed to the scale effect of elastic properties shown in Fig. 7, which increases the stiffness by 20 % at 60 degrees. For the imperfect models, the compliance is similar with a clear change in density distribution. Process-induced defects for each cell topology influence the optimized material distribution. The Tetrahedron-based topology contains struts that are oriented at 0 (horizontal, over melted), 45 (diagonal, with decreased over melting) and 90 degrees (vertical, undersized) with respect to the building direction. These manufacturing defects, which are strongly dependent on the strut orientation [36], are different for both rotation angles. Hence, they alter the density distribution over the fixed beam.

In the case of the L-shaped beam shown in Fig. 11, similarly due to small discrepancies in elastic properties (E_{xx} and G_{xy}) of as-designed and imperfect models, a small change is noticed in the density distribution for unit cells tessellated along the build direction (top). The compliance of the imperfect model is found to be 25 % higher than that of the as-designed model. At 60 degrees (bottom), the difference in density distribution is more obvious; the structure of the imperfect model is more porous in the bottom bar and near the location where the load is applied.

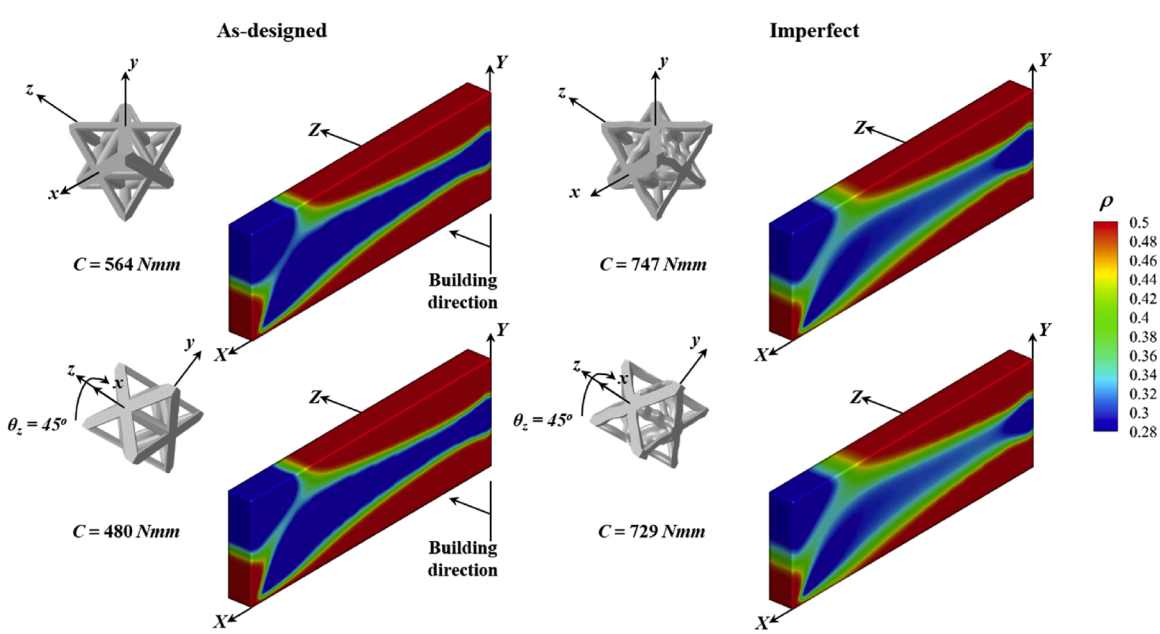

Fig. 12. Optimized relative density distribution for the fixed-beam benchmark problem, of as-designed versus imperfect models using the Octet-truss topology. Top: unit cells rotated with an angle 0°, and bottom: unit cells rotated with an angle 45° around the *z*-axis.

In addition, its compliance is 21 % higher compared to the as-designed model. Similarly, comparing the as-designed models at dissimilar unit cell orientations shows that the compliance is 10 % higher at rotation angle 0 with approximately uniform density distribution. For the imperfect models, where cell topology plays a significant role in manufacturing defects, the structure features a different density distribution and higher porosity at 60 degrees, while the compliance is 14 % higher for unit cells tessellated along the building direction.

3.2. Octet-truss topology

Figs. 12 and 13 pertain to the results provided by the Octet-truss cell for the benchmark problems. For both cases (fixed-beam and L-shaped beam), unit cell orientations are selected at rotation angles 0 (top) and 45 degrees (bottom) around the z-axis. The two orientations are selected in an identical fashion to those for the Tetrahedron-based cell; one along the build direction and the other at the orientation that features the maximum discrepancy in Young's moduli found along the x direction, ($\Delta(E_{xx}/E_s)_{\max} = 25\%$ shown in Fig. 8). Unlike the tetrahedron-based unit cell, the discrepancy in elastic properties appears in all orientations and along given directions. Along the build direction, there is approximately 14 % difference in Young's modulus E_{xx} and 35 % difference in shear modulus G_{xy}, between as-designed and imperfect models. In both benchmark problems, dissimilar relative density distributions are found at the two cell orientations. For the imperfect models, lower porosity is noticed in the middle region of the fixed beam, while it is higher for the L-Shape beam in the bottom bar regions and close to the location of the applied load. In terms of compliance, the imperfect models are typically less stiff than the as-designed models. For fixed-beams, their compliance is 32 % and 52 % higher at unit cell orientations of 0 and 45 degrees respectively. For the L-shape beams, the compliance is higher by 35 % and 46 % at given orientations respectively.

Similarly, by analyzing the as-designed models at the two cell orientations, we can notice that the density distribution is equivalent with compliance 15 % and 14 % higher at 0 degrees for fixed-beam and L-shaped beam problems respectively. This is due to the higher stiffness (20 %) of unit cells at 45 degrees than those oriented along the build direction. For the fixed-beam problem using imperfect models, the change in compliance and density distribution is mild. This might be due to the small discrepancy noticed in elastic and shear moduli between the two orientations ($\Delta(E_{xx}/E_s) = 6\%$ and $\Delta(G_{xy}/G_s) = 11\%$). However, for the L-shaped beam problems under other loading and boundary conditions, the change in relative density is evident with 7% higher compliance at rotation angle 0. The reason may be attributed to manufacturing defects, reported to be dependent on strut orientation and cell topology [36]; these influence the material distribution and compliance of the structure. The Octet-truss cell has over melted struts oriented at 0 degrees (horizontal), and struts with decreased over melting at 45 degrees (diagonal) to the building direction.

The observations above point out the role of manufacturing defects, unit cell orientation, and cell topology on the mechanics discrepancy, and their effect on both compliance and optimized density distribution of cellular structures. From the results, we gather that the compliance of the optimized structure is affected by the elasticity tensor that is rescaled by changing the rotation angle of the building block. As per the density distributions, the difference within the design domain is demonstrated to be proportional to the discrepancy in elastic properties resisting deformation under the specific loading and boundary conditions of each problem.

While promising, this work has a number of limitations. First, only some geometric defects were here examined through defect quantification. Others, of course, exist, such as mass agglomeration at the strut joints, surface roughness caused by attached beads of un-melted powder, and other material defects. Their dispersion needs to be quantified and their role on the mechanics and optimized density distribution assessed. Besides, further work is required to compare the results obtained with the methodology presented in this work and other existing approaches for robust topology optimization. Second, the issue of incomplete tessellation for unit cells close to the boundary of the design domain has not been considered. Finally, this work has studied lattice materials with a set of prescribed unit cell orientations, i.e. the unit cells do not change their angle within the design domain. Future work is needed to optimize

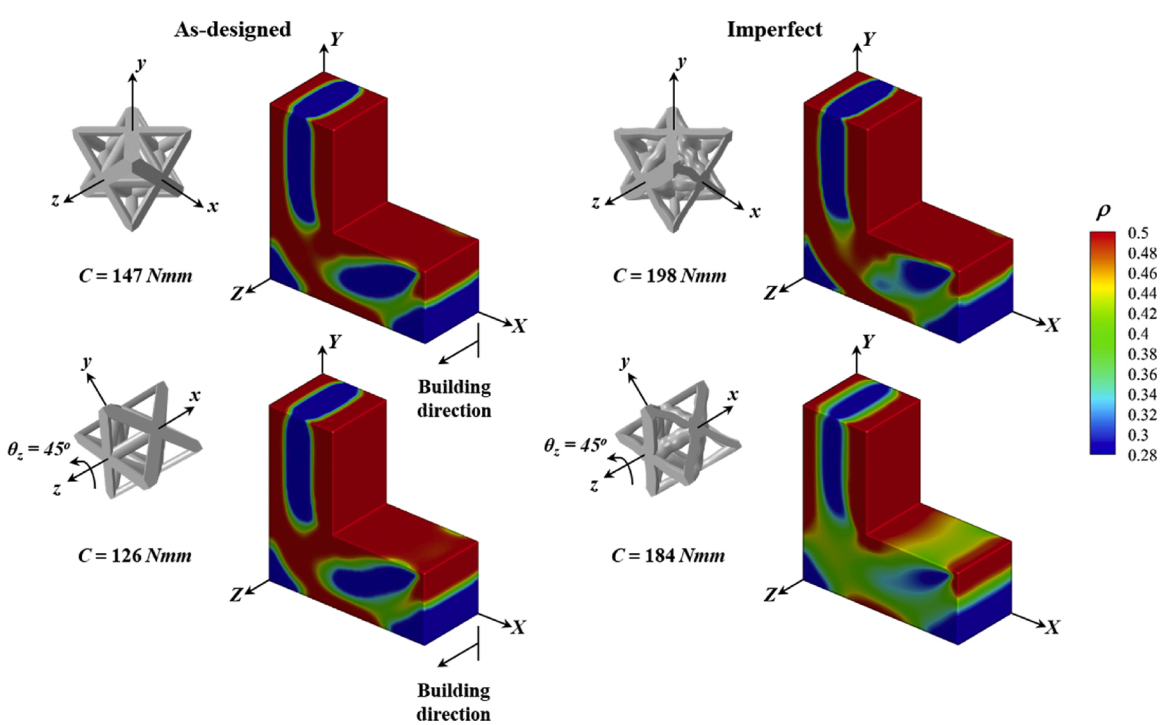

Fig. 13. Optimized relative density distribution for the L-shaped beam benchmark problem, of as-designed versus imperfect models using the Octet-truss topology. Top: unit cells rotated with an angle 0°, and bottom: unit cells rotated with an angle 45° around the z-axis.

the design of lattices with differently oriented cells [90–92]. Further work is needed to address these points in the future.

4. Conclusions

This work has presented a general framework to assess the role of geometric imperfections on the mechanics and topology optimization of additively built lattice materials. The methodology has been applied for demonstrative purposes to two unit cells satisfying given geometric constraints. The results have shown the role of cell orientation and manufacturing defects, which impart unit cell anisotropy and impact mechanical properties. For the Tetrahedron-based unit cell, a maximum discrepancy in Young's modulus of 23 % is observed at an angle of 60 degrees around the build direction, while for Octet-truss unit cells, the maximum difference of 25 % is observed at 45 degrees. As for the influence on the compliance and optimized relative density distribution, the difference within the design domain of each problem is shown to be proportional to the discrepancy in elastic properties between as-built and defect-free microarchitectures. The current study emphasizes the importance of including process-induced geometric defects during the design process of lattice structure, since doing so gives a more realistic picture of their structural performance. Future work involves the experimental validation of the optimized structures here obtained for imperfect lattice materials.

Author statement

Ahmed Moussa: Developed the finite element model, developed the framework of the topology optimization problem, performed the simulation, edited the figures, and wrote and edited the manuscript.

David Melancon: Rebuilt STL model from CT images, developed the scheme for defect extraction, conducted the SEM, and edited the text.

Asma El Elmi: Contributed to the mechanical properties calculations and edited the text.

Damiano Pasini: Contributed to the methodology and supervised the research through the entire process by providing continuous technical and scientific advice on every aspect of the work. He also edited the figures and the text.

Declaration of Competing Interest

The authors report no declarations of interest.

Acknowledgements

The authors acknowledge funding from the Natural Sciences and Engineering Research Council of Canada through the Discovery Grant Program and the Network for Holistic Innovation in Additive Manufacturing.

Appendix

Supplementary material related to this article can be found, in the online version, at doi:https://doi.org/10.1016/j.addma.2020.101608.

References

[1] X. Zheng, W. Smith, J. Jackson, B. Moran, H. Cui, D. Chen, J. Ye, N. Fang, N. Rodriguez, T. Weisgraber, C.M. Spadaccini, Multiscale metallic metamaterials, Nat. Mater. 15 (10) (2016) 1100–1106.
[2] M.G. Lee, J.W. Lee, S.C. Han, K. Kang, Mechanical analyses of "Shellular", an ultralow-density material, Acta Mater. 103 (2016) 595–607.
[3] J.K. Guest, J.H. Prévost, Optimizing multifunctional materials: design of microstructures for maximized stiffness and fluid permeability, Int. J. Solids Struct. 43 (22–23) (2006) 7028–7047.
[4] N.M.A. Palumbo, C.W. Smith, W. Miller, K.E. Evans, Near-zero thermal expansivity 2-D lattice structures: performance in terms of mass and mechanical properties, Acta Mater. 59 (6) (2011) 2392–2403.
[5] T.J. Lu, H.A. Stone, M.F. Ashby, Heat transfer in open-cell metal foams, Acta Mater. 46 (10) (1998) 3619–3635.
[6] P. Wang, J. Shim, K. Bertoldi, Effects of geometric and material nonlinearities on tunable band gaps and low-frequency directionality of phononic crystals, Phys. Rev. B 88 (1) (2013) 014304.
[7] H. Kang, C.-Y. Lin, S.J. Hollister, Topology optimization of three dimensional tissue engineering scaffold architectures for prescribed bulk modulus and diffusivity, Struct. Multidiscip. Optim. 42 (4) (2010) 633–644.
[8] V.J. Challis, J.K. Guest, J.F. Grotowski, A.P. Roberts, Computationally generated cross-property bounds for stiffness and fluid permeability using topology optimization, Int. J. Solids Struct. 49 (23–24) (2012) 3397–3408.
[9] S. Arabnejad Khanoki, D. Pasini, Multiscale design and multiobjective optimization of orthopaedic cellular hip implants, in: IDETC 2011: ASME 2011 International Design Engineering Technical Conferences (IDETC) and Computers and Information in Engineering Conference (CIE), Washington, DC, USA: ASME, 2011.
[10] S. Arabnejad, B. Johnston, M. Tanzer, D. Pasini, Fully porous 3D printed titanium femoral stem to reduce stress-shielding following total hip arthroplasty, J. Orthop. Res. 35 (8) (2017) 1774–1783.
[11] A. Moussa, M. Tanzer, D. Pasini, Cervical fusion cage computationally optimized with porous architected Titanium for minimized subsidence, J. Mech. Behav. Biomed. Mater. 85 (2018) 134–151.
[12] L.E. Murr, S.M. Gaytan, F. Medina, H. Lopez, E. Martinez, B.I. Machado, D. H. Hernandez, L. Martinez, M.I. Lopez, R.B. Wicker, J. Bracke, Next-generation biomedical implants using additive manufacturing of complex, cellular and functional mesh arrays, Philos. Trans. Math. Phys. Eng. Sci. 368 (1917) (2010) 1999–2032.
[13] J.M. Sobral, S.G. Caridade, R.A. Sousa, J.F. Mano, R.L. Reis, Three-dimensional plotted scaffolds with controlled pore size gradients: effect of scaffold geometry on mechanical performance and cell seeding efficiency, Acta Biomater. 7 (3) (2011) 1009–1018.
[14] D. Pasini, J.K. Guest, Imperfect architected materials: mechanics and topology optimization, MRS Bull. 44 (10) (2019) 766–772.
[15] L. Zhao, S. Ha, K.W. Sharp, A.B. Geltmacher, R.W. Fonda, A.H. Kinsey, Y. Zhang, S. M. Ryan, D. Erdeniz, D.C. Dunand, K.J. Hemker, J.K. Guest, T.P. Weihs, Permeability measurements and modeling of topology-optimized metallic 3-D woven lattices, Acta Mater. 81 (2014) 326–336.
[16] S. Lin, L. Zhao, J.K. Guest, T.P. Weihs, Z. Liu, Topology optimization of fixed-geometry fluid diodes, J. Mech. Des. 137 (8) (2015) 081402.
[17] B. Levine, A new era in porous metals: applications in orthopaedics, Adv. Eng. Mater. 10 (9) (2008) 788–792.
[18] S. Bose, S. Vahabzadeh, A. Bandyopadhyay, Bone tissue engineering using 3D printing, Mater. Today 16 (12) (2013) 496–504.
[19] L. Liu, P. Kamm, F. García-Moreno, J. Banhart, D. Pasini, Elastic and failure response of imperfect three-dimensional metallic lattices: the role of geometric defects induced by Selective Laser Melting, J. Mech. Phys. Solids 107 (2017) 160–184.
[20] P. Wang, H. Lei, X. Zhu, H. Chen, D. Fang, Influence of manufacturing geometric defects on the mechanical properties of AlSi10Mg alloy fabricated by selective laser melting, J. Alloys Compd. 789 (2019) 852–859.
[21] A. Ferrigno, F. Di Caprio, R. Borrelli, F. Auricchio, A. Vigliotti, The mechanical strength of Ti-6Al-4V columns with regular octet microstructure manufactured by electron beam melting, Materialia 5 (2019) 100232.
[22] R. Wauthle, J. van der Stok, S. Amin Yavari, J. Van Humbeeck, J.-P. Kruth, A. A. Zadpoor, H. Weinans, M. Mulier, J. Schrooten, Additively manufactured porous tantalum implants, Acta Biomater. 14 (2015) 217–225.
[23] D. Melancon, Z. Bagheri, R. Johnston, L. Liu, M. Tanzer, D. Pasini, Mechanical characterization of structurally porous biomaterials built via additive manufacturing: experiments, predictive models, and design maps for load-bearing bone replacement implants, Acta Biomater. 63 (2017) 350–368.
[24] A.H. Glassman, J.D. Bobyn, M. Tanzer, New femoral designs: do they influence stress shielding? Clin. Orthop. Relat. Res. 453 (2006) 64–74.
[25] J.D. Bobyn, E.S. Mortimer, A.H. Glassman, C.A. Engh, J.E. Miller, C.E. Brooks, Producing and avoiding stress shielding. Laboratory and clinical observations of noncemented total hip arthroplasty, Clin. Orthop. Relat. Res. (274) (1992) 79–96.
[26] A. Rahimizadeh, Z. Nourmohammadi, S. Arabnejad, M. Tanzer, D. Pasini, Porous architected biomaterial for a tibial-knee implant with minimum bone resorption and bone-implant interface micromotion, J. Mech. Behav. Biomed. Mater. 78 (2018) 465–479.
[27] A. Maggi, H. Li, J.R. Greer, Three-dimensional nano-architected scaffolds with tunable stiffness for efficient bone tissue growth, Acta Biomater. 63 (2017) 294–305.
[28] A. Gross, P. Pantidis, K. Bertoldi, S. Gerasimidis, Correlation between topology and elastic properties of imperfect truss-lattice materials, J. Mech. Phys. Solids 124 (2019) 577–598.
[29] D.D. Symons, N.A. Fleck, The imperfection sensitivity of isotropic two-dimensional elastic lattices, J. Appl. Mech. 75 (5) (2008), p. 051011-051011-051018.
[30] C. Chen, T.J. Lu, N.A. Fleck, Effect of imperfections on the yielding of two-dimensional foams, J. Mech. Phys. Solids 47 (11) (1999) 2235–2272.
[31] W. Ronan, V.S. Deshpande, N.A. Fleck, The tensile ductility of cellular solids: the role of imperfections, Int. J. Solids Struct. 102–103 (2016) 200–213.
[32] H.C. Tankasala, V.S. Deshpande, N.A. Fleck, Tensile response of elastoplastic lattices at finite strain, J. Mech. Phys. Solids 109 (2017) 307–330.
[33] N.A. Fleck, X. Qiu, The damage tolerance of elastic–brittle, two-dimensional isotropic lattices, J. Mech. Phys. Solids 55 (3) (2007) 562–588.
[34] N.E.R. Romijn, N.A. Fleck, The fracture toughness of planar lattices: imperfection sensitivity, J. Mech. Phys. Solids 55 (12) (2007) 2538–2564.

[35] E. Hernández-Nava, C.J. Smith, F. Derguti, S. Tammas-Williams, F. Leonard, P. J. Withers, I. Todd, R. Goodall, The effect of defects on the mechanical response of Ti-6Al-4V cubic lattice structures fabricated by electron beam melting, Acta Mater. 108 (2016) 279–292.
[36] Z.S. Bagheri, D. Melancon, L. Liu, R.B. Johnston, D. Pasini, Compensation strategy to reduce geometry and mechanics mismatches in porous biomaterials built with Selective Laser Melting, J. Mech. Behav. Biomed. Mater. 70 (2017) 17–27.
[37] M. Dallago, S. Raghavendra, V. Luchin, G. Zappini, D. Pasini, M. Benedetti, Geometric assessment of lattice materials built via Selective Laser Melting, Mater. Today Proc. 7 (2019) 353–361.
[38] M. Dallago, B. Winiarski, F. Zanini, S. Carmignato, M. Benedetti, On the effect of geometrical imperfections and defects on the fatigue strength of cellular lattice structures additively manufactured via Selective Laser Melting, Int. J. Fatigue 124 (2019) 348–360.
[39] J. Mueller, K. Shea, Buckling, build orientation, and scaling effects in 3D printed lattices, Mater. Today Commun. 17 (2018) 69–75.
[40] H. Lei, C. Li, J. Meng, H. Zhou, Y. Liu, X. Zhang, P. Wang, D. Fang, Evaluation of compressive properties of SLM-fabricated multi-layer lattice structures by experimental test and μ-CT-based finite element analysis, Mater. Des. 169 (2019) 107685.
[41] J. Parthasarathy, B. Starly, S. Raman, A. Christensen, Mechanical evaluation of porous titanium (Ti6Al4V) structures with electron beam melting (EBM), J. Mech. Behav. Biomed. Mater. 3 (3) (2010) 249–259.
[42] M. Mahbod, M. Asgari, Elastic and plastic characterization of a new developed additively manufactured functionally graded porous lattice structure: analytical and numerical models, Int. J. Mech. Sci. 155 (2019) 248–266.
[43] M. Dallago, F. Zanini, S. Carmignato, D. Pasini, M. Benedetti, Effect of the geometrical defectiveness on the mechanical properties of SLM biomedical Ti6Al4V lattices, Procedia Struct. Integr. 13 (2018) 161–167.
[44] S.M. Ahmadi, R. Hedayati, Y. Li, K. Lietaert, N. Tümer, A. Fatemi, C.D. Rans, B. Pouran, H. Weinans, A.A. Zadpoor, Fatigue performance of additively manufactured meta-biomaterials: the effects of topology and material type, Acta Biomater. 65 (2018) 292–304.
[45] B. Van Hooreweder, Y. Apers, K. Lietaert, J.-P. Kruth, Improving the fatigue performance of porous metallic biomaterials produced by Selective Laser Melting, Acta Biomater. 47 (2017) 193–202.
[46] R. Wauthle, S.M. Ahmadi, S. Amin Yavari, M. Mulier, A.A. Zadpoor, H. Weinans, J. Van Humbeeck, J.P. Kruth, J. Schrooten, Revival of pure titanium for dynamically loaded porous implants using additive manufacturing, Mater. Sci. Eng. C Mater. Biol. Appl. 54 (2015) 94–100.
[47] C.R. Thomsen, F. Wang, O. Sigmund, Buckling strength topology optimization of 2D periodic materials based on linearized bifurcation analysis, Comput. Methods Appl. Mech. Eng. 339 (2018) 115–136.
[48] X. Huang, Y.M. Xie, Optimal design of periodic structures using evolutionary topology optimization, Struct. Multidiscip. Optim. 36 (6) (2008) 597–606.
[49] Z. Wu, L. Xia, S. Wang, T. Shi, Topology optimization of hierarchical lattice structures with substructuring, Comput. Methods Appl. Mech. Eng. 345 (2019) 602–617.
[50] Y. Chen, S. Zhou, Q. Li, Multiobjective topology optimization for finite periodic structures, Comput. Struct. 88 (11–12) (2010) 806–811.
[51] A. Moussa, S. Rahman, M. Xu, M. Tanzer, D. Pasini, Topology optimization of 3D-printed structurally porous cage for acetabular reinforcement in total hip arthroplasty, J. Mech. Behav. Biomed. Mater. 105 (2020) 103705.
[52] B. Yi, Y. Zhou, G.H. Yoon, K. Saitou, Topology optimization of functionally-graded lattice structures with buckling constraints, Comput. Methods Appl. Mech. Eng. 354 (2019) 593–619.
[53] M.M. Neves, O. Sigmund, M.P. Bendsøe, Topology optimization of periodic microstructures with a penalization of highly localized buckling modes, Int. J. Numer. Methods Eng. 54 (6) (2002) 809–834.
[54] L. Cheng, J. Bai, A.C. To, Functionally graded lattice structure topology optimization for the design of additive manufactured components with stress constraints, Comput. Methods Appl. Mech. Eng. 344 (2019) 334–359.
[55] D. Pasini, A. Moussa, A. Rahimizadeh, Stress-constrained topology optimization for lattice materials, in: H. Altenbach, A. Öchsner (Eds.), Encyclopedia of Continuum Mechanics, Springer Berlin Heidelberg, Berlin, Heidelberg, 2018, pp. 1–19.
[56] J.K. Guest, T. Igusa, Structural optimization under uncertain loads and nodal locations, Comput. Methods Appl. Mech. Eng. 198 (1) (2008) 116–124.
[57] C.C. Seepersad, J.K. Allen, D.L. McDowell, F. Mistree, Robust design of cellular materials with topological and dimensional imperfections, J. Mech. Des. 128 (6) (2006) 1285–1297.
[58] O. Amir, O. Sigmund, B.S. Lazarov, M. Schevenels, Efficient reanalysis techniques for robust topology optimization, Comput. Methods Appl. Mech. Eng. 245–246 (0) (2012) 217–231.
[59] F. Wang, B. Lazarov, O. Sigmund, On projection methods, convergence and robust formulations in topology optimization, Struct. Multidiscip. Optim. 43 (6) (2011) 767–784.
[60] E. Andreassen, B.S. Lazarov, O. Sigmund, Design of manufacturable 3D extremal elastic microstructure, Mech. Mater. 69 (1) (2014) 1–10.
[61] O. Sigmund, Manufacturing tolerant topology optimization, Acta Mech. Sin. 25 (2) (2009) 227–239.
[62] R.M. Gorguluarslan, A multi-level upscaling and validation framework for uncertainty quantification in additively manufactured lattice structures. Mechanical Engineering, Georgia Institute of Technology, 2016.
[63] Y.-C. Chan, K. Shintani, W. Chen, Robust topology optimization of multi-material lattice structures under material and load uncertainties, Front. Mech. Eng. 14 (2) (2019) 141–152.
[64] S. Arabnejad, R. Burnett Johnston, J.A. Pura, B. Singh, M. Tanzer, D. Pasini, High-strength porous biomaterials for bone replacement: a strategy to assess the interplay between cell morphology, mechanical properties, bone ingrowth and manufacturing constraints, Acta Biomater. 30 (2016) 345–356.
[65] S. Arabnejad, D. Pasini, Mechanical properties of lattice materials via asymptotic homogenization and comparison with alternative homogenization methods, Int. J. Mech. Sci. 77 (2013) 249–262.
[66] M.P. Bendsøe, O. Sigmund, Topology Optimization: Theory, Methods, and Applications, Springer, Berlin; New York, 2003.
[67] K. Svanberg, The method of moving asymptotes—a new method for structural optimization, Int. J. Numer. Methods Eng. 24 (2) (1987) 359–373.
[68] T.E. Bruns, D.A. Tortorelli, Topology optimization of non-linear elastic structures and compliant mechanisms, Comput. Methods Appl. Mech. Eng. 190 (26–27) (2001) 3443–3459.
[69] V.S. Deshpande, M.F. Ashby, N.A. Fleck, Foam topology: bending versus stretching dominated architectures, Acta Mater. 49 (6) (2001) 1035–1040.
[70] P. Heinl, L. Müller, C. Körner, R.F. Singer, F.A. Müller, Cellular Ti–6Al–4V structures with interconnected macro porosity for bone implants fabricated by selective electron beam melting, Acta Biomater. 4 (5) (2008) 1536–1544.
[71] O.L.A. Harrysson, O. Cansizoglu, D.J. Marcellin-Little, D.R. Cormier, H.A. West, Direct metal fabrication of titanium implants with tailored materials and mechanical properties using electron beam melting technology, Mater. Sci. Eng. C 28 (3) (2008) 366–373.
[72] Paul A. Yushkevich, Joseph Piven, Heather Cody Hazlett, Rachel Gimpel Smith, Sean Ho, James C. Gee, a.G. Gerig, User-guided 3D active contour segmentation of anatomical structures: Significantly improved efficiency and reliability, Neuroimage 31 (3) (2006) 1116–1128.
[73] M.P. Wand, M.C. Jones, Kernel smoothing. Monographs on Statistics and Applied Probability, first ed., Chapman & Hall, London, 1995.
[74] B.H. Hassani, E., A review of homogenization and topology optimization I-homogenization theory for media with periodic structure, Comput. Struct. 69 (6) (1997) 707–717.
[75] S.J.K.N. Hollister, A comparison of homogenization and standard mechanics analyses for periodic porous composites, Comput. Mech. 10 (2) (1992) 73–95.
[76] Y. Wang, S. Arabnejad, M. Tanzer, D. Pasini, Hip implant design with three-dimensional porous architecture of optimized graded density, J. Mech. Des. 140 (11) (2018) 111406.
[77] S. Arabnejad, B. Johnston, M. Tanzer, D. Pasini, Fully porous 3D printed titanium femoral stem to reduce stress-shielding following total hip arthroplasty, J. Orthop. Res. 35 (8) (2017) 1774–1783.
[78] Y. Cai, L. Xu, G. Cheng, Novel numerical implementation of asymptotic homogenization method for periodic plate structures, Int. J. Solids Struct. 51 (1) (2014) 284–292.
[79] H. Tollenaere, D. Caillerie, Continuous modeling of lattice structures by homogenization, Adv. Eng. Softw. 29 (7) (1998) 699–705.
[80] Renishaw, Ti6Al4V ELI-0406 Powder for Additive Manufacturing, 2016.
[81] H.-G. Beyer, B. Sendhoff, Robust optimization – a comprehensive survey, Comput. Methods Appl. Mech. Eng. 196 (33–34) (2007) 3190–3218.
[82] M. Schevenels, B.S. Lazarov, O. Sigmund, Robust topology optimization accounting for spatially varying manufacturing errors, Comput. Methods Appl. Mech. Eng. 200 (49–52) (2011) 3613–3627.
[83] M. Jansen, G. Lombaert, M. Diehl, B. Lazarov, O. Sigmund, M. Schevenels, Robust topology optimization accounting for misplacement of material, Struct. Multidiscip. Optim. 47 (3) (2013) 317–333.
[84] M. Jansen, G. Lombaert, M. Schevenels, Robust topology optimization of structures with imperfect geometry based on geometric nonlinear analysis, Comput. Methods Appl. Mech. Eng. 285 (0) (2015) 452–467.
[85] B.S. Lazarov, M. Schevenels, O. Sigmund, Robust design of large-displacement compliant mechanisms, Mech. Sci. 2 (2) (2011) 175–182.
[86] A. Díaz, O. Sigmund, Checkerboard patterns in layout optimization, Struct. Optim. 10 (1) (1995) 40–45.
[87] O. Sigmund, J. Petersson, Numerical instabilities in topology optimization: a survey on procedures dealing with checkerboards, mesh-dependencies and local minima, Struct. Optim. 16 (1) (1998) 68–75.
[88] O. Sigmund, Morphology-based black and white filters for topology optimization, Struct. Multidiscip. Optim. 33 (4–5) (2007) 401–424.
[89] E. Andreassen, A. Clausen, M. Schevenels, B. Lazarov, O. Sigmund, Efficient topology optimization in MATLAB using 88 lines of code, Struct. Multidiscip. Optim. 43 (1) (2011) 1–16.
[90] P. Geoffroy-Donders, G. Allaire, O. Pantz, 3-d topology optimization of modulated and oriented periodic microstructures by the homogenization method, J. Comput. Phys. 401 (2020) 108994.
[91] J.P. Groen, F.C. Stutz, N. Aage, J.A. Bærentzen, O. Sigmund, De-homogenization of optimal multi-scale 3D topologies, Comput. Methods Appl. Mech. Eng. 364 (2020) 112979.
[92] J.P. Groen, J. Wu, O. Sigmund, Homogenization-based stiffness optimization and projection of 2D coated structures with orthotropic infill, Comput. Methods Appl. Mech. Eng. 349 (2019) 722–742.